

Three-dimensional localization of ultracold atoms in an optical disordered potential

F. Jendrzejewski¹, A. Bernard¹, K. Müller¹, P. Cheinet¹, V. Josse^{1*}, M. Piraud¹, L. Pezzé¹, L. Sanchez-Palencia¹, A. Aspect¹ and P. Bouyer^{1,2}

In disordered media, quantum interference effects are expected to induce complete suppression of electron conduction. The phenomenon, known as Anderson localization, has a counterpart with classical waves that has been observed in acoustics, electromagnetism and optics, but a direct observation for particles remains elusive. Here, we report the observation of the three-dimensional localization of ultracold atoms in a disordered potential created by a speckle laser field. A phenomenological analysis of our data distinguishes a localized component of the resulting density profile from a diffusive component. The observed localization cannot be interpreted as the classical trapping of particles with energy below the classical percolation threshold in the disorder, nor can it be understood as quantum trapping in local potential minima. Instead, our data are compatible with the self-consistent theory of Anderson localization tailored to our system, involving a heuristic energy shift that offers scope for future interpretation.

Anderson localization (AL) was proposed more than 50 years ago¹ to understand how disorder can lead to the total cancellation of electron conduction in certain materials. It is a purely quantum, one-particle effect, which can be interpreted as due to interference between the various amplitudes associated with the scattering paths of a matter wave propagating among impurities². According to the celebrated scaling theory³, AL depends on the dimension, and in the three-dimensional (3D) case a mobility edge is predicted. It is an energy threshold separating localized states, which decay to zero at infinity and correspond to insulators, from extended states, which correspond to conductors. However, determining the precise value of the mobility edge, and the corresponding critical behaviour around it, remains a challenge for microscopic theory, numerical simulations, and experiments². The quest for AL has been pursued not only in condensed matter physics⁴, but also in wave physics⁵, and experiments have been carried out with light waves^{6–9}, microwaves^{10,11} and acoustic waves¹². Following theoretical proposals^{13–18}, recent experiments have shown that ultracold atoms in optical disorder constitute a remarkable system to study 1D localization^{19,20} or 2D diffusion^{21,22} of matter waves in real space (see refs 23,24 for recent reviews). Cold atoms in a ‘kicked rotor’ situation have also been used to demonstrate 1D dynamical localization²⁵, that is, localization in p -space, and to study a mapping of 3D AL in that space²⁶. Here, we report the observation of 3D localization of ultracold atoms of a Bose–Einstein condensate (BEC), suspended against gravity, and released in a 3D optical disordered potential with short correlation lengths in all directions. Fluorescence imaging of the expanding cloud yields density profiles composed of a steady localized part and a diffusive part. A phenomenological analysis allows us to determine the localized fraction and the diffusion coefficients of the diffusing part. The localization we observe cannot be interpreted as classical trapping of particles with energy below the classical

percolation threshold in the disorder, which is well below the average energy of the atoms. Similarly, quantum trapping in local potential minima is excluded, because the local potential wells are too tight to support stationary states with energy less than the potential well depth. In contrast, our observations are compatible with the self-consistent theory of AL (ref. 27), taking into account the specific features of the experiment, in particular the broad energy distribution of the atoms placed in the disordered potential, provided we introduce a heuristic energy shift whose interpretation remains to be elucidated.

Experimental scheme

Our scheme (Fig. 1a), described in more detail in the Methods section, is a generalization of the one that allowed us to demonstrate AL in 1D (refs 15,19). It starts with a dilute BEC with several 10^4 atoms of ⁸⁷Rb, initially in a shallow quasi-isotropic optical trap. It is in thermal equilibrium, with about the same number of uncondensed atoms. When the trap is switched off, the atoms are kept suspended against gravity by a magnetic field gradient. Monitoring the free expansion of the suspended atomic cloud, we obtain the values of the initial chemical potential μ_{in} ($\mu_{\text{in}}/h \simeq 40$ Hz, where h is the Planck constant) and the temperature ($T \sim 1$ nK).

To study localization, an optical disorder is switched on, in less than 100 μs , at time $t_i = 50$ ms after release. At that time, the atom–atom interaction energy E_{int} , estimated from the observed atomic density, has become negligible ($E_{\text{int}}/h \sim 1$ Hz) compared with the disorder amplitude (see below). The disordered potential $V(\mathbf{r})$ is created by the coherent addition of two crossed speckle laser fields^{28,29} with the same polarization. It is repulsive with an exponential probability distribution $\mathcal{P}(V) = V_{\text{R}}^{-1} \exp(-V/V_{\text{R}})$. The potential amplitude, V_{R} , is equal both to the average value of the potential and its standard deviation. It can be varied from 0 up to $V_{\text{R}}/h = 1.1$ kHz. Figure 1b shows an example of a specific realization

¹Laboratoire Charles Fabry Unité Mixte de Recherche 8501, Institut d’Optique, Centre National de la Recherche Scientifique, Université Paris-Sud 11, 2 Avenue Augustin Fresnel, 91127 Palaiseau cedex, France, ²Laboratoire Photonique, Numérique et Nanosciences Unité Mixte de Recherche 5298, Université Bordeaux 1, Institut d’Optique and Centre National de la Recherche Scientifique, 351 cours de la Libération, 33405 Talence, France.

*e-mail: vincent.josse@institutoptique.fr.

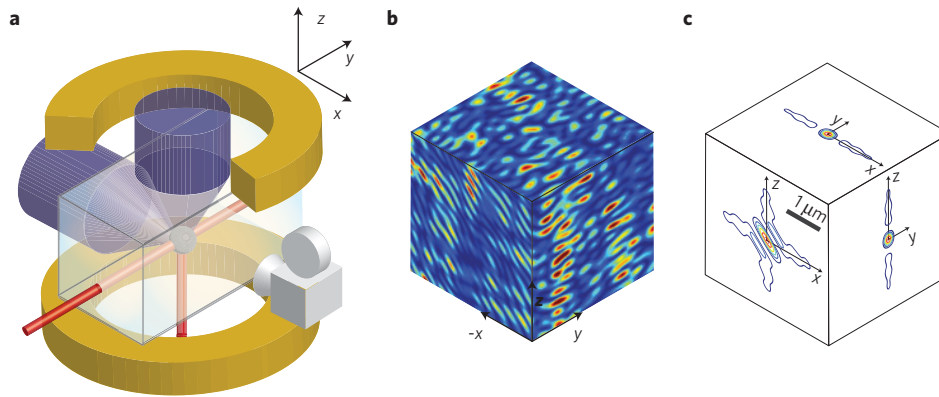


Figure 1 | Experiment. **a**, A dilute BEC of ultracold ^{87}Rb atoms, initially trapped by the red-detuned crossed laser beams, is released and subjected to a repulsive disordered potential. This potential is realized by the optical speckle field produced by two crossed, blue-detuned, coherent laser beams passed through diffusive plates and focused on the atoms. The (paramagnetic) atoms are suspended against gravity by a magnetic field gradient (produced by the yellow coils), and the expansion of the atomic cloud can be observed for times as long as 6 s. The EMCCD camera images the fluorescence produced by a resonant probe, and yields the atomic column density integrated along the x axis. **b**, False colour representation of a realization of the disordered potential in the $x = 0$, $y = 0$ and $z = 0$ planes. **c**, Plots of the 3D autocorrelation function of the disordered potential in the $x = 0$, $y = 0$ and $z = 0$ planes (the equal level lines represent levels separated by 14% of the maximum value).

of the speckle potential. The random spatial distribution has an anisotropic autocorrelation function (Fig. 1c). A 3D Gaussian fit of the central peak of the autocorrelation function yields standard radii of $0.11\ \mu\text{m}$, $0.27\ \mu\text{m}$ and $0.08\ \mu\text{m}$, along the main axes (axis y and the two bisecting lines of x - z). For such a disordered potential, the classical percolation threshold is less than $10^{-2}V_R$, eliminating the possibility of classical trapping of the atoms, which have a typical energy of the order of V_R (see Methods). Moreover, the correlation energy¹⁷ $E_R = \hbar^2/m\sigma_R^2$ (where $\sigma_R \simeq 0.13\ \mu\text{m}$ is the geometric average of the standard radii of the autocorrelation function, m the atom mass and $\hbar = h/2\pi$ the reduced Planck constant) is larger than the disorder amplitudes V_R used in the experiment ($E_R/h = 6.5\ \text{kHz}$). Then, the local minima of the disordered potential do not support bound states, eliminating the possibility of quantum trapping in individual local minima.

We observe the atomic cloud, at a given time t , by direct *in situ* fluorescence imaging along the x axis (see Methods). This yields the column density $\bar{n}(y, z, t) = \int dx n(x, y, z, t)$ (where $n(x, y, z, t)$ is the 3D atomic density). The obtained profiles have small residual spatial fluctuations (Fig. 2a), which do not depend on the particular realization of the laser speckle disorder. This can be traced to the averaging arising from the finite spatial resolution ($15\ \mu\text{m}$, FWHM) of the imaging system, and it is consistent with the fact that each profile is a sum of many profiles associated with different atom energy components that probe different, uncorrelated, k -components of the disordered potential. One can then consider that the observed profiles represent, within the experimental accuracy, an ensemble average over different realizations of the disorder.

We have studied how the expansion of the released atomic cloud is affected when we apply the laser speckle potential. Figure 2a shows the evolution of the observed column density profiles for two different values of the disorder amplitude V_R . For the smaller value ($V_R/h = 135\ \text{Hz}$), we observe a diffusive expansion (Fig. 2b). After 1.2 s, the density at the centre has decreased so much that the atomic cloud is no longer measurable. In contrast, for the larger value of the disorder amplitude ($V_R/h = 680\ \text{Hz}$), the diffusive expansion is slower (Fig. 2b), and an almost steady peak survives at the centre for observation times as long as 6 s (Fig. 2c).

Phenomenological analysis of the data

To analyse these observations, we use a phenomenological model, assuming that the observed profiles are the sum of two contributions: (1) a steady localized part that is the replica of the

initial profile $\bar{n}_i(y, z)$, that is, the BEC and its thermal wings at $t = t_i$; (2) a diffusive expanding part $\bar{n}_D(y, z, t)$, whose contribution at the centre decays towards zero. More precisely, we assume that we can decompose the observed column density as

$$\bar{n}(y, z, t) = f_{\text{loc}} \times \bar{n}_i(y, z) + \bar{n}_D(y, z, t) \quad (1)$$

This decomposition is supported by the observation (Fig. 2b) that the measured rms sizes Δu , along the $u \in \{y, z\}$ axes, of the column density profiles, vary as $\Delta u(t)^2 = \Delta u(t_i)^2 + 2\langle D^u \rangle (t - t_i)$. Linear fits allow us to measure the diffusion coefficients $\langle D^y \rangle$ and $\langle D^z \rangle$. The brackets indicate an average over the energy distribution of the atoms. Figure 2c shows that the column density at the centre tends asymptotically towards a finite value, which is determined by a fit to the function $\bar{n}(0, 0, t)/\bar{n}_i(0, 0) = A + B(t - t_i)^{-1}$, where A refers to the localized part. The $(t - t_i)^{-1}$ evolution is expected for a diffusive behaviour of the column density at the centre when the size of the initial profile is negligible. It results from the integration over one dimension of the $(t - t_i)^{-3/2}$ evolution expected for the 3D density at the origin. Finally, as we will see below, theory predicts that the localization lengths are smaller than the resolution of the images, so that the profile of the localized part is a replica of the initial profile, hence the form chosen for the first term in equation (1). The constant A of the fit is then interpreted as the localized fraction of atoms, f_{loc} . It is found to be equal to 21% for $V_R/h = 680\ \text{Hz}$, and 1% for $V_R/h = 135\ \text{Hz}$. In the absence of disorder ($V_R = 0$), we fit the central density by $A + B(t - t_i)^{-2}$, as expected for a ballistic expansion, and find $A = 0$, that is, a null localized fraction.

The phenomenological analysis of the experimental data described above has been carried out for different values of V_R . Figure 3 shows that the localized fraction, which is vanishingly small at very weak disorder, increases rapidly with V_R above $V_R/h \sim 135\ \text{Hz}$, and reaches a nearly saturated value slightly larger than 20% at $V_R/h \sim 500\ \text{Hz}$. Note that inhomogeneous atom losses (see Methods) entail an overestimation of the condensed fraction for $V_R/h < 400\ \text{Hz}$, so that correcting for it would result in an even steeper increase of the observed condensed fraction. Similarly, Fig. 4 shows that the measured average diffusion coefficients, $\langle D^u \rangle$, exhibit a steep decrease with the disorder amplitude V_R around the value at which a localized fraction appears, and reach almost constant values at $V_R/h \sim 500\ \text{Hz}$. These values of a few $\hbar/3m$ are of the order of what is expected just above the mobility edge¹⁷.

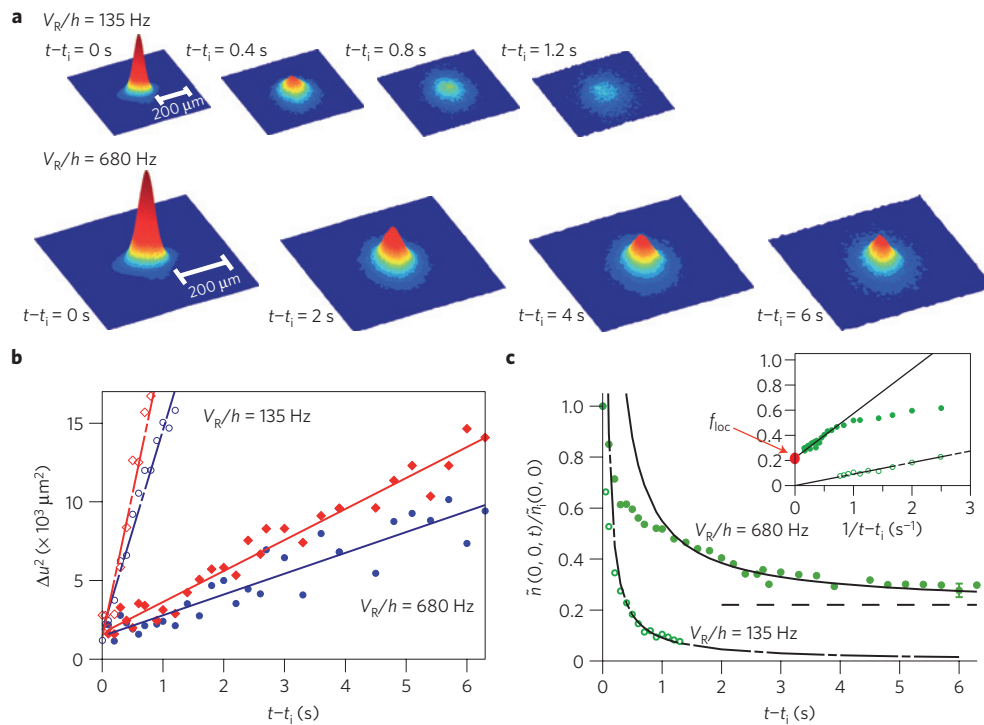


Figure 2 | Evolution of the atomic cloud for two different amplitudes of the disorder. **a**, Plots of the column density in the y - z plane, as observed by fluorescence imaging along the x axis (Fig. 1a) at various delays $t - t_i$ after application of the disorder. For a weak disorder ($V_R/h = 135$ Hz), we observe an expansion leading to the disappearance of any observable atomic density for times larger than 1.2 s. For a strong disorder ($V_R/h = 680$ Hz), the atomic cloud is still clearly visible after 6 s, and the profile shows a steady peak around the origin, superposed on a slowly expanding component. As shown in Fig. 2b, the expanding parts have a diffusive behaviour in both cases. **b**, Time evolution of the mean squared widths along y (blue circles) and z (red diamonds) of the column density profiles, and their fits by straight lines, yielding the diffusion coefficients along y and z . The anisotropy of the disorder, visible on Fig. 1b, is reflected on the diffusion coefficients. **c**, Time evolution of the column density at the centre (green circles). The black line is a fit by the function $A + B/(t - t_i)$, where the asymptotic value A is interpreted as the localized fraction f_{loc} (see text). The inset shows the same data plotted as a function of $1/(t - t_i)$, fitted by the black straight line whose intercept on the left axis yields f_{loc} .

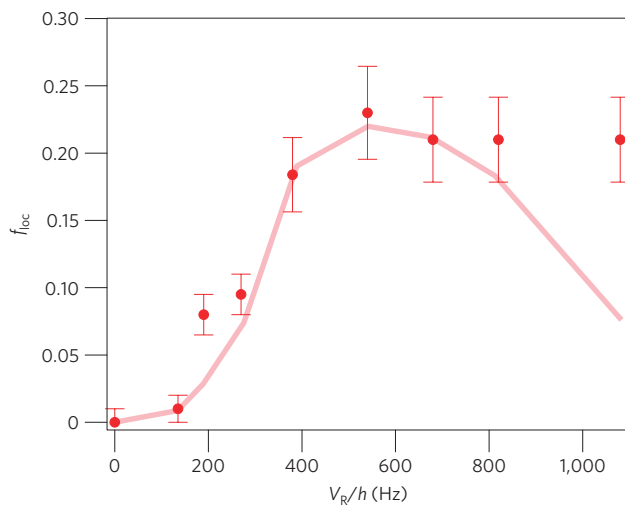


Figure 3 | Localized fraction versus disorder amplitude. The points give the localized fraction f_{loc} determined from the decay of the central density (Fig. 2c). The error bars reflect the uncertainty on each individual fit and the fluctuations from shot to shot. The solid line shows the results of the theoretical calculation, including the heuristic relative energy shift explained in the text.

Theoretical description

We now compare the results of the phenomenological analysis of the experimental data with the theory of quantum transport and

AL specifically applied to our situation, that is, taking into account: (1) the spatial extension of the atomic gas at the initial time t_i ; (2) its energy distribution induced by the sudden application of the disordered potential at time t_i ; (3) the anisotropy of the 3D speckle potential. We write the spatial density of the atomic gas as^{15,16,18}

$$n(\mathbf{r}, t) = \int d\mathbf{r}_i \int dE \mathcal{D}_i(\mathbf{r}_i, E) P(\mathbf{r} - \mathbf{r}_i, t - t_i | E) \quad (2)$$

where $\mathcal{D}_i(\mathbf{r}, E)$ represents the semi-classical joint position–energy density just after the time t_i when the speckle potential is switched on, and $P(\mathbf{r} - \mathbf{r}_i, t - t_i | E)$ is the (anisotropic) probability of quantum transport, that is, the probability distribution that a particle of energy E , placed at point \mathbf{r}_i at time t_i , is found at point \mathbf{r} at time t .

The function $P(\mathbf{r}, t | E)$, whose character changes from localized to extended when the energy passes the mobility edge E_c , plays the central role in AL. We calculate it self-consistently within the on-shell Born approximation^{27,30}, using the same method as in ref. 31, except that here we do not include the real part of the self-energy (see Methods). It provides the mobility edge E_c and the expressions of the probability of quantum transport^{30,31}. Within the above approximation, we find $E_c - V_R \approx 1.6 V_R^2 / E_R$ for our experimental parameters (for example, $[E_c - V_R]/h = 4.5$ Hz and 108 Hz for $V_R/h = 135$ Hz and 680 Hz respectively). In the AL regime ($E < E_c$), $P(\mathbf{r} | E)$ is a static, anisotropic, exponentially localized function, characterized by the localization tensor $\mathbf{L}_{loc}(E)$. In the diffusive regime ($E > E_c$), $P(\mathbf{r} | E)$ is a time-dependent, anisotropic, Gaussian function, characterized by the self-consistent diffusion tensor $\mathbf{D}_*(E)$. In the case where the range of atomic energies extends

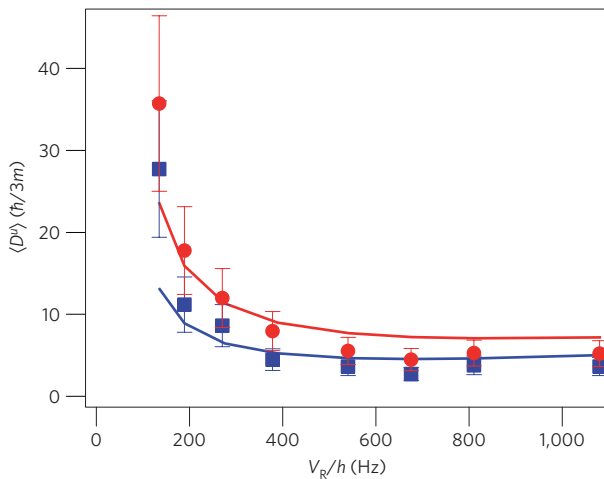


Figure 4 | Diffusion coefficient versus disorder amplitude. The blue squares and red circles give the diffusion coefficients, $\langle D^u \rangle$, in units of $\hbar/3m$, along the $u = y, z$ axes, respectively. These coefficients are derived from the evolution of the mean squared widths of the atomic cloud (Fig. 2b). The error bars reflect the effect of background noise on the mean squared widths. The solid blue (y) and red (z) lines show the results of the theoretical calculation of these coefficients, using the same heuristic energy shift as in Fig. 3.

below and above the mobility edge, both expressions of $P(\mathbf{r}, t|E)$ (equations (3) and (4) in Methods) play a role in the integral of equation (2), leading respectively to a localized component and a diffusing component.

To calculate $\mathcal{D}_i(\mathbf{r}, E)$, we use the fact that the sudden application of the disorder (in $\sim 100\mu\text{s}$ in the experiment) at time t_i hardly affects the density profile, $n_i(\mathbf{r})$, but significantly modifies the energy distribution because the disorder is strong (for example, $V_R^2/E_R \simeq \mu_{\text{in}}$ for $V_R/h \simeq 500$ Hz). We thus assume, for simplicity, separation of the position and energy variables, so that $\mathcal{D}_i(\mathbf{r}, E) = n_i(\mathbf{r}) \times f_i(E)$. The initial density profile $n_i(\mathbf{r})$ is determined from fits to the measured density profile at time t_i (upper panels in Fig. 5). On the other hand, we have no simple experimental method for determining precisely the energy distribution $f_i(E)$ of the atoms in the disorder, and we calculate it numerically (see Methods). We find that $f_i(E)$ is peaked around V_R (the average value of the disordered potential) with a width ΔE_{f_i} ranging from $\Delta E_{f_i}/h \sim 20$ Hz (for $V_R/h = 135$ Hz) to $\Delta E_{f_i}/h \sim 140$ Hz (for $V_R/h = 680$ Hz).

As expected, the calculation of the localized functions shows that the localization lengths (the components of $\mathbf{L}_{\text{loc}}(E)$) increase with the energy and diverge at the mobility edge E_c . Except in a narrow window ΔE below E_c (for example, $\Delta E/h \sim 20$ Hz for $V_R/h = 680$ Hz), however, they remain smaller than the imaging resolution ($15\mu\text{m}$), and much smaller than the size of the atomic cloud when the disorder is switched on (Fig. 5). As most of the energy components are outside that window, we make $P(\mathbf{r}|E) \simeq \delta(\mathbf{r})$ for $E < E_c$. This yields a localized profile, which is simply a replica of the initial profile $\tilde{n}_i(y, z)$, supporting the form chosen for the first term in equation (1) used for the phenomenological analysis.

The calculated localized fraction is given by $f_{\text{loc}} = \int_{-\infty}^{E_c} dE f_i(E)$. When we perform this calculation, we find numerical results significantly larger than the measured values. Actually, simple inspection shows that the numerical value found for f_{loc} is extremely sensitive to the numerical accuracy in the determination of $f_i(E)$ as well as to any approximation in the theoretical calculations of E_c . It is also very sensitive to uncertainties in experimental parameters, in particular the amplitude V_R and the details of the disordered potential. Considering all these uncertainties, we tried to

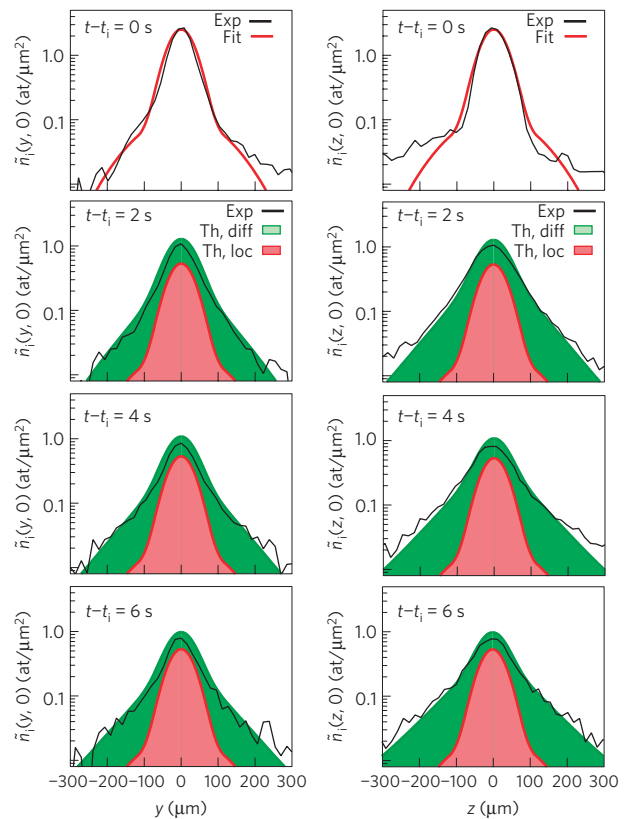


Figure 5 | Evolution of the density profiles in a strong disorder

($V_R/h = 680$ Hz): experiment versus theory. The figure shows cuts of the column density profiles along y ($\tilde{n}(y, 0, t)$, left column) and z ($\tilde{n}(z, 0, t)$, right column), at various delays after application of the disorder. The solid black lines are the experimental data. In the top panels (corresponding to the initial time $t = t_i$ when the disorder is switched on), the solid red lines are fits to the data. In all other panels (corresponding to $t > t_i$), the solid red lines are these fitted initial profiles multiplied by the localized fraction $f_{\text{loc}} = 0.21$, hence describing the localized part. Adding the theoretically determined diffusive parts at various delays, we obtain the green profiles, which reproduce well the experimental profiles.

introduce into the calculation of f_{loc} a heuristic energy shift ΔE_{heur} between the energy functionals $f_i(E)$ and $P(\mathbf{r}|E)$, and we found that a relative shift of the form $\Delta E_{\text{heur}} = 3.35V_R^2/E_R$ (for example, $\Delta E_{\text{heur}}/h \sim 225$ Hz for $V_R/h = 680$ Hz) leads to a fair agreement with the experimental results (Fig. 3). Note that ΔE_{heur} is approximately twice as large as $E_c - V_R$ and the width of the energy distribution ΔE_{f_i} . It thus strongly affects the value of f_{loc} .

The calculation of the diffusion coefficients involves the energy components with $E > E_c$. For consistency, we use the same energy shift as introduced in the calculation of the localized fraction, that is, we write $\langle D^u \rangle = \int_{E_c}^{+\infty} dE f_i(E - \Delta E_{\text{heur}}) \hat{\mathbf{u}} \cdot \mathbf{D}_*(E) \cdot \hat{\mathbf{u}}$, where $\hat{\mathbf{u}}$ is the unit vector pointing along the $u \in \{y, z\}$ axis. As shown in Fig. 4, we then find a fair agreement between the results of this calculation and the experimental data. In particular, the anisotropy of the diffusion tensor is reproduced well. Note that the theoretical calculations do not involve any free parameter, apart from the heuristic energy shift discussed above.

Figure 5 shows the comparison between the theoretical and experimental profiles, at various delays, in the case $V_R/h = 680$ Hz. The theoretical profiles represent equation (2), where $\mathcal{D}_i(\mathbf{r}, E)$ and $P(\mathbf{r}, t|E)$ are calculated as explained above. These theoretical profiles are composed of a localized part (replica of the initial profile multiplied by the calculated localized fraction; red line), plus an evolving diffusive part (the green line is the sum of the two parts).

The fair agreement with experimental profiles at various delays shows the consistency of our theoretical analysis (including the heuristic energy shift) with the experimental observations.

This theoretical description of our experimental situation allows us to interpret the behaviour of f_{loc} (Fig. 3) and $\langle D^u \rangle$ (Fig. 4) as resulting from the competition of two effects when V_R increases. On the one hand, for each energy component, the incoherent (Boltzmann) mean free path $l_B(E)$, and thus the diffusion coefficient $D^u(E)$, decrease. According to the (on-shell) Ioffe–Regel criterion for localization³², $k_E l_B(E) \lesssim 1$ (where $k_E = \sqrt{2mE}/\hbar$ is the typical particle wave vector at energy E), the mobility edge E_c then increases, so that f_{loc} increases if the atom energy distribution is unchanged. This effect dominates for weak disorder ($V_R \lesssim 400$ Hz). On the other hand, the atom energy distribution width and the heuristic shift increase with V_R , so as to populate increasingly the diffusive component. The two effects counterbalance each other and the localized fraction reaches a maximum, while the average diffusion coefficients reach almost constant values.

Discussion and outlook

It is natural to ask whether our observation of a localized component can be interpreted as 3D AL, and whether the separation between the localized and diffusive components corresponds to the mobility edge. Recall that our observations are incompatible with classical trapping, owing to the very low value of the percolation threshold, or with quantum trapping, because our disorder does not support bound states. Therefore, we know of no other explanation than AL for our observations. Moreover, the self-consistent theory of AL applied to the exact experimental situation yields good quantitative agreement with the experimental results, provided we use the energy distribution of the atoms, which is strongly modified by the sudden application of the disorder, and displace it by a heuristic shift. The comparison is, however, too sensitive to uncertainties in the experimental parameters and to approximations in the theory to be considered fully quantitative. Such a definitive comparison would be of utmost interest, the experiment then being a test-bed for theories of AL, and several future advances towards that goal can be envisaged.

On the theoretical side, it will be important to clarify the status of the heuristic energy shift. On one hand, its simple form ($\propto V_R^2$) suggests that it may be partially due to some disregarded term at Born first order, for instance the shift of energy states that is not taken into account in the on-shell approximation of the self-consistent theory of AL, but which might be significant^{31,33}. On the other hand, the above form of the shift may be too simple, as suggested by the discrepancy with experimental data obtained at the highest values of V_R in Fig. 3. The search for a more elaborate form may lead to a better understanding of the localization phenomenon we have observed.

On the experimental side, it would be interesting to be able to release, in the disordered potential, a sample of atoms with a narrow energy distribution, controlled at will. It would then be possible to explore the localization transition, in particular to measure the exact value of the mobility edge E_c , and to study the critical behaviour, permitting a comparison with existing theoretical treatments and hopefully suggesting routes for theoretical improvements. Beyond such developments on AL of non-interacting atoms, future experiments will include the addition of controlled interactions between atoms, because the effect of interactions on AL is an open problem of great interest, in particular in 3D (refs 4,24).

Note added in proof. During the preparation of this manuscript, we were made aware of a related work, reporting localization of fermions in a speckle potential³⁴.

Methods

BEC and magnetic levitation. The initial BEC contains several 10^4 atoms of ^{87}Rb in the $|F=2, m_F=-2\rangle$ ground state, in thermal equilibrium with about the same

number of uncondensed atoms. It is created in a shallow quasi-isotropic Gaussian optical trap of trapping frequencies $\omega/2\pi \sim 5$ Hz. The initial chemical potential μ_{in} and temperature are determined by monitoring the free expansion of the atomic cloud in the presence of the suspending potential (realized by the magnetic field gradient). The maximum velocity $v_{\text{max}} \sim 0.5$ mm s⁻¹ in the expanding BEC corresponds to an initial chemical potential of $\mu_{\text{in}} = 3mv_{\text{max}}^2/4 \simeq 40$ Hz $\times h$. The velocity distribution of the thermal component has a rms width of ~ 0.3 mm s⁻¹, that is, corresponding to a temperature of $T \sim 1$ nK ($k_B T/h \sim 20$ Hz, where k_B is the Boltzmann constant).

The suspending potential has a repulsive and isotropic component of the form $-m\omega^2 r^2/2$, with $\omega \simeq 1.8$ s⁻¹. The weak expelling force resulting from this potential is responsible for spatially inhomogeneous losses that play a role only when the expansion is large (weak or null disorder). When the expansion is small enough (strong disorder, corresponding to the points at $V_R/h \geq 400$ Hz in Figs 2–5), the inhomogeneous losses are negligible compared with the observed homogeneous losses, characterized by an inverse decay time constant of ~ 0.14 s⁻¹. In the quantitative analysis, we compensate the losses by rescaling our data to a fixed total number of atoms.

Observation of the atomic profiles. We use a high-sensitivity Electron Multiplying Charge Coupled Device (EMCCD) camera to image, along the x axis, the fluorescence obtained when applying, for 50 μs , a saturating resonant probe on the atomic cloud, at a chosen time t . The overall transverse resolution is 15 μm (full-width at half-maximum) in the y – z plane, resulting from both the finite resolution of the imaging system and a numerical sliding average. The obtained column density profile is averaged over three to five recordings to increase the signal-to-noise ratio.

3D speckle disorder and classical percolation threshold. To create a homogeneous 3D disorder with small correlation lengths along all directions of space, we cross two coherent orthogonal speckle fields with a width of 2.4 mm (at $1/e^2$), large compared with the extension of the atomic cloud. The laser is significantly blue-detuned (wavelength of 532 nm as compared to the ^{87}Rb resonance wavelength of 780 nm), so that the disordered potential is repulsive, and spontaneous emission is negligible. The two crossed speckle fields have the same polarization (along the y axis), yielding a Gaussian random amplitude distribution^{28,29}, hence the exponential distribution quoted in the text for the disordered potential.

We have numerically evaluated the percolation threshold E_p of our 3D speckle potential, that is, the energy such that all classical particles with energy $E < E_p$ are trapped in finite-size allowed regions. Using various values of the grid step, the numerical calculations provide an upper bound for the percolation threshold, $E_p \leq 4(1) \times 10^{-3} V_R$. Above E_p , the fraction of classical trapping regions is found to vanish for $E \geq 8(1) \times 10^{-3} V_R$. Using the energy distribution $f_i(E)$ calculated numerically, with or without the heuristic energy shift, we find that the fraction of classically trapped particles is negligible ($\ll 1\%$). This is a major advantage of using two coherent crossed speckles, rather than two speckles with orthogonal polarizations, or two incoherent speckles, for which the field amplitude distribution would not be Gaussian. In the case of perpendicularly polarized speckles, the numerical calculation indeed yields a much larger percolation threshold $E_p \simeq 0.18(1)V_R$.

Probability of quantum transport. The function $P(\mathbf{r}, t|E)$ is calculated using the on-shell self-consistent theory^{27,30}. The incoherent (Boltzmann) diffusion tensor is first calculated using microscopic quantum transport theory applied to our 3D anisotropic speckle potential. The quantum interference terms are then incorporated in the form of the Cooperon and Hikami contributions. This provides an equation for the dynamic, quantum-corrected diffusion tensor, $\mathbf{D}_*(E, \Omega)$. Solving the latter self-consistently in the long time limit (that is, the low frequency limit $\Omega \rightarrow 0$) with an appropriate short-distance cut-off^{17,27,31}, we obtain the mobility edge E_c and explicit expressions for $P(\mathbf{r}, t|E)$. In the AL regime ($E < E_c$),

$$P(\mathbf{r}|E) = \frac{\exp\left(-\sqrt{\mathbf{r} \cdot \mathbf{L}_{\text{loc}}^{-2}(E) \cdot \mathbf{r}}\right)}{4\pi \det\{\mathbf{L}_{\text{loc}}(E)\} \sqrt{\mathbf{r} \cdot \mathbf{L}_{\text{loc}}^{-2}(E) \cdot \mathbf{r}}} \quad (3)$$

is a static, anisotropic, exponentially localized function, characterized by the localization tensor $\mathbf{L}_{\text{loc}}(E)$. In the diffusive regime ($E > E_c$),

$$P(\mathbf{r}, t|E) = \frac{\exp(-\mathbf{r} \cdot \mathbf{D}_*^{-1}(E) \cdot \mathbf{r}/4t)}{\sqrt{(4\pi t)^3 \det\{\mathbf{D}_*(E)\}}} \quad (4)$$

is a time-dependent, anisotropic, Gaussian function, characterized by the self-consistent diffusion tensor $\mathbf{D}_*(E)$.

Energy distribution. When the initial chemical potential of the BEC (μ_{in}) and the thermal energy ($k_B T$) are smaller than the disorder parameters, the energy distribution can be approximated by $f_i(E) \simeq A(\mathbf{k}=0, E)$, where $A(\mathbf{k}, E) = \langle \mathbf{k} | \delta(E - H) | \mathbf{k} \rangle$ is the spectral function of the disordered medium, with $H = -\hbar^2 \nabla^2 / 2m + V(\mathbf{r})$ the non-interacting Hamiltonian associated with a realization of the disordered potential $V(\mathbf{r})$. To calculate $A(\mathbf{k}=0, E)$, we decompose the operator $\delta(E - H)$ onto the energy eigenbasis, as obtained by direct numerical

diagonalization of the Hamiltonian H . The numerical results are obtained in a box of linear length $\sim 15\lambda$ and of grid step $\sim 0.2\lambda$ ($\lambda = 532$ nm is the laser wavelength). The disorder average is performed over 100 realizations of $V(\mathbf{r})$ using the parameters of the 3D speckle potential used in the experiments.

Received 29 July 2011; accepted 7 February 2012; published online 4 March 2012

References

- Anderson, P. W. Absence of diffusion in certain random lattices. *Phys. Rev.* **109**, 1492–1505 (1958).
- Lagendijk, A., Van Tiggelen, B. A. & Wiersma, D. Fifty years of Anderson localization. *Phys. Today* **62**, 24–29 (August 2009).
- Abrahams, E., Anderson, P. W., Licciardello, D. C. & Ramakrishnan, T. V. Scaling theory of localization: Absence of quantum diffusion in two dimensions. *Phys. Rev. Lett.* **42**, 673–676 (1979).
- Lee, P. A. & Ramakrishnan, T. V. Disordered electronic systems. *Rev. Mod. Phys.* **57**, 287–337 (1985).
- Van Tiggelen, B. A. in *Mathematical and Physical Sciences* Vol. 531 (ed. Fouque, J.) 1–60 (Nato Advanced Science Institutes Series, Series C, Addison Wesley, 1999).
- Wiersma, D. S., Bartolini, P., Lagendijk, A. & Righini, R. Localization of light in a disordered medium. *Nature* **390**, 671–673 (1997).
- Störzer, M., Gross, P., Aegerter, C. M. & Maret, G. Observation of the critical regime near Anderson localization of light. *Phys. Rev. Lett.* **96**, 063904 (2006).
- Schwartz, T., Bartal, G., Fishman, S. & Segev, M. Transport and Anderson localization in disordered two-dimensional photonic lattices. *Nature* **446**, 52–55 (2007).
- Lahini, Y. *et al.* Anderson localization and nonlinearity in one-dimensional disordered photonic lattices. *Phys. Rev. Lett.* **100**, 013906 (2008).
- Dalichaouch, R., Armstrong, J. P., Schultz, S., Platzman, P. M. & McCall, S. L. Microwave localization by 2-dimensional random scattering. *Nature* **354**, 53–55 (1991).
- Chabanov, A. A., Stoytchev, M. & Genack, A. Z. Statistical signatures of photon localization. *Nature* **404**, 850–853 (2000).
- Hu, H., Strybulevych, A., Page, J. H., Skipetrov, S. E. & Van Tiggelen, B. A. Localization of ultrasound in a three-dimensional elastic network. *Nature Phys.* **4**, 845–848 (2008).
- Damski, B., Zakrzewski, J., Santos, L., Zoller, P. & Lewenstein, M. Atomic Bose and Anderson glasses in optical lattices. *Phys. Rev. Lett.* **91**, 080403 (2003).
- Roth, R. & Burnett, K. Phase diagram of bosonic atoms in two-color superlattices. *Phys. Rev. A* **68**, 023604 (2003).
- Sanchez-Palencia, L. *et al.* Anderson localization of expanding Bose–Einstein condensates in random potentials. *Phys. Rev. Lett.* **98**, 210401 (2007).
- Piraud, M., Lugan, P., Bouyer, P., Aspect, A. & Sanchez-Palencia, L. Localization of a matter wave packet in a disordered potential. *Phys. Rev. A* **83**, 031603 (2011).
- Kuhn, R. C., Sigwarth, O., Miniatura, C., Delande, D. & Müller, C. A. Coherent matter wave transport in speckle potentials. *New J. Phys.* **9**, 161 (2007).
- Skipetrov, S. E., Minguzzi, A., Van Tiggelen, B. A. & Shapiro, B. Anderson localization of a Bose–Einstein condensate in a 3D random potential. *Phys. Rev. Lett.* **100**, 165301 (2008).
- Billy, J. *et al.* Direct observation of Anderson localization of matter waves in a controlled disorder. *Nature* **453**, 891–894 (2008).
- Roati, G. *et al.* Anderson localization of a non-interacting Bose–Einstein condensate. *Nature* **453**, 895–898 (2008).
- Robert-de-Saint-Vincent, M. *et al.* Anisotropic 2D diffusive expansion of ultracold atoms in a disordered potential. *Phys. Rev. Lett.* **104**, 220602 (2010).
- Pezzé, L. *et al.* Regimes of classical transport of cold gases in a two-dimensional anisotropic disorder. *New J. Phys.* **13**, 095015 (2011).
- Aspect, A. & Inguscio, M. Anderson localization of ultracold atoms. *Phys. Today* **62**, 30–35 (August 2009).
- Sanchez-Palencia, L. & Lewenstein, M. Disordered quantum gases under control. *Nature Phys.* **6**, 87–95 (2010).
- Moore, F. L., Robinson, J. C., Bharucha, C., Williams, P. E. & Raizen, M. G. Observation of dynamical localization in atomic momentum transfer: A new testing ground for quantum chaos. *Phys. Rev. Lett.* **73**, 2974–2977 (1994).
- Chabé, J. *et al.* Experimental observation of the Anderson metal–insulator transition with atomic matter waves. *Phys. Rev. Lett.* **101**, 255702 (2008).
- Vollhardt, D. & Wölfle, P. in *Electronic Phase Transitions* (eds Hanke, W. & Kopalev, Y.) 1 (Elsevier, 1992).
- Clément, D. *et al.* Experimental study of the transport of coherent interacting matter-waves in a 1D random potential induced by laser speckle. *New J. Phys.* **8**, 165 (2006).
- Goodman, J. W. *Speckle Phenomena in Optics: Theory and Applications* (Roberts, 2007).
- Wölfle, P. & Bhatt, R. N. Electron localization in anisotropic systems. *Phys. Rev. B* **30**, 3542–3544 (1984).
- Piraud, M., Pezzé, L. & Sanchez-Palencia, L. Matter wave transport and Anderson localization in anisotropic 3D disorder. Preprint at <http://arxiv.org/abs/1112.2859v1> (2011).
- Ioffe, A. F. & Regel, A. R. Non crystalline, amorphous, and liquid electronic semiconductors. *Prog. Semicond.* **4**, 237–291 (1960).
- Yedjour, A. & Van Tiggelen, B. A. Diffusion and localization of cold atoms in 3D optical speckle. *Eur. Phys. J. D* **59**, 249–255 (2010).
- Kondov, S. S., McGehee, W. R., Zirbel, J. J. & DeMarco, B. Three-dimensional Anderson localization of ultracold fermionic matter. *Science* **333**, 66–68 (2011).

Acknowledgements

We thank S. Seidel and V. Volchkov for experimental contributions, M. Besbes for assistance on numerical calculations, M. Lecrivain for helping design and realize the suspending coils, A. Villing and F. Moron for assistance with the electronics, and T. Giamarchi and B. van Tiggelen for fruitful discussions. This research was supported by the European Research Council (Starting grant ‘ALoGlaDis’, FP7/2007–2013 Grant Agreement No. 256294, and Advanced grant ‘Quantatop’), the Agence Nationale de la Recherche (ANR-08-blan-0016-01), the Ministère de l’Enseignement Supérieur et de la Recherche, the Délégation Générale de l’Armement, the Triangle de la Physique and the Institut Francilien de Recherche sur les Atomes Froids. We acknowledge the use of the computing facility cluster Grappe massivement parallèle de calcul scientifique of the LUMière MATière research federation (Fédération de Recherche LUMière MATière 2764).

Author contributions

All authors have contributed equally.

Additional information

The authors declare no competing financial interests. Reprints and permissions information is available online at www.nature.com/reprints. Correspondence and requests for materials should be addressed to V.J.